Axisymmetric flow simulations of fiber suspensions as described by 3D probability distribution function

Julien Ferec, Dihya Mezi, Suresh Advani, Gilles Ausias

Version of Record: https://www.sciencedirect.com/science/article/pii/S0377025720301300
Manuscript_7b08360e16bc1b3c527d473978080e70

Axisymmetric flow simulations of fiber suspensions as described by 3D probability distribution function

Julien Férec[a,*], Dihya Mezi[a], Suresh G. Advani[b], Gilles Ausias[a]

[a]Univ. Bretagne Sud, UMR CNRS 6027, IRDL, F-56100 Lorient, France
[b]Department of Mechanical Engineering, Center for Composite Materials, University of Delaware, 101 Academy Street, Newark, DE 19716, USA

Abstract

Numerical models are developed to examine fiber suspension flows through axisymmetric geometries, such as a circular pipe, a center-gated disk and a die exit. The fiber orientation micro-structure is fully described by using the entire probability distribution function (PDF) in 3D instead of the second and fourth moments of the PDF, which introduce errors due to the closure approximation when using orientation tensor descriptions. A Newtonian suspending fluid is considered for the constitutive relationship and simulations are performed with and without coupling the flow and fiber orientation. Results are compared with numerical simulations obtained by using the standard evolution equation for the second-order orientation tensor and the IBOF closure approximation. It is found that the IBOF closure approximation does a relatively good job of matching the exact orientation results given by the probability distribution function. For the three explored flows, the difference between the predicted orientation results using the coupled and decoupled approaches is not significant. There is a noticeable difference in the velocity field solutions, specifically at the die exit where the coupled approach increases the die swell ratio when the fibers enter the inlet with random orientation state.

Keywords: Fiber suspension; Polymer composite; Fiber orientation; Numerical modeling; Probability distribution function; Axisymmetric flow

1. Introduction

In this work, a numerical simulation of fiber suspension flows in axisymmetric geometries is developed. Rheology of fiber suspensions is significantly influenced by the orientation state of the fibers and a key point is to choose how to describe this orientation state. In engineering applications, a large range of flow dimensions are involved from millimeters which is the average gap for short fiber filled melted thermoplastics in processes such as injection molding to a meter long in steel fiber filled fresh concrete used to construct buildings. On a smaller scale, fillers are used to cover a broad range of dimensions from the nanometer scale (i.e., carbon nanotubes) to the millimeter scale (i.e., metallic fibers in reinforced concrete). It should also be noted that fibers are often added in large quantities. The number of fibers in the field of study is therefore extremely large and it is not practical to follow the fiber dynamics of each and every fiber. Instead of examining fibers individually, a representative elementary volume (REV) is introduced to investigate the behavior for a composite material element that contains a fixed number of fibers. This number is large enough, typically a few hundred, to be representative.

Since fiber orientation is a key parameter, a fiber statistic descriptor in the REV must be specified. Thus, the orientation of a fiber population in the REV is described by a probability distribution function (PDF),

*julien.ferec@univ-ubs.fr

$\psi(\mathbf{x}, \mathbf{p}, t)$. It represents the probability of finding at a time t and at the position $\mathbf{x}$ a fiber oriented in the solid angle $d\mathbf{p}$ about the orientation $\mathbf{p}$, where $\mathbf{p}$ is the unit vector parallel to the fiber axis. In 3D flow, $\mathbf{p}$ can take all the directions on a unit sphere. In 2D planar flow, the PDF is reduced to a circle and $d\mathbf{p}$ becomes an angle. In 2D axisymmetric flows, sometimes elongational flow can occur in the plane perpendicular to the rz-plane, in which case the PDF must be described on a sphere as for 3D flows. The PDF can realistically represent the real state of orientation with the fiber population in the RVE. The accuracy depends on the number of unknowns used to represent the PDF. Thus in 2D plane, if $d\mathbf{p}$ is equal to 5 degrees then the number of unknowns is 72 and if $d\mathbf{p}$ is equal to 0.1 degree, the number of unknowns balloons to 3600. In 3D this number can be at least one order of magnitude higher.

Far from the solid wall, in a Newtonian fluid and in a dilute regime, the fiber center of mass is supposed to translate at the same velocity as that of the surrounding fluid and its orientation evolution is described by the well-known Jeffery equation [1]. This equation can be introduced in the Fokker-Planck equation which gives the time rate of change of the PDF. If fibers are introduced in a fluid, its behavior is modified. Dinh and Armstrong [2] proposed a constitutive equation for a Newtonian fluid containing fibers with an infinite aspect ratio. Then, they extended it for a population of fibers in a REV using a PDF. Thus, a comprehensive model is constituted of governing equation(s) to describe the fiber dynamics, derived from the Fokker-Planck equation, and the constitutive equation that describes the suspension rheology based on PDF.

In the 80's when the first computers were used to solve fluid mechanics problems, the use of hundreds of unknowns for PDF at each node was impractical. Therefore, Advani and Tucker [3] defined the second- and fourth-order orientation tensors (the second and fourth moments of the PDF), which reduce drastically the number of unknowns to 5 in 3D, 4 in 2D axisymmetric and 2 in 2D planar flows. Although the fourth-order orientation tensors could capture the influence on mechanical and rheological behavior, major drawback of converting the evolution equation for the PDF to orientation tensors requires a closure approximation in the equation and therefore, the unanswered question is does the use of orientation tensors cause a significant inaccuracy in the model. However, models for fiber suspensions based on orientation tensors are widely used since the 80's and have also found their application in injection and compression molding simulations (Moldflow, Autodesk, Inc., San Rafael, CA or Moldex3D, CoreTech System Co., Ltd., Taipei, China). It should also be noted that Jeffery's equation and Dinh and Armstrong model are based on the following hypothesis: Newtonian fluid, semi-concentrated regime and rigid particles [4].

Orientation tensors have been very helpful in developing models with a linear matrix behavior, without fiber interactions and without wall effects. On the other hand, the use of tensors in the presence of non-linearity or discontinuity seems more complex or sometimes impossible. Thus, Férec et al. [5] developed a model for fiber interactions where their statistics are described by tensors called interaction tensors [6]. Their use is complicated due to the need to complete the model with new closure approximations [7]. Deriving macroscopic models which employ orientation tensors for non-Newtonian matrices also poses problems. For shear-thinning fluids, tensors describing fiber orientation have a complex form as it includes a deformation mode dependence [8]. In the case of viscoelastic matrices in the limit of low Deborah number, the use of the sixth-order orientation tensor is required [9, 10]. The use of tensor is efficient and convenient, but they have three drawbacks. The first one is the loss of physics, the second one is the need to use a closure approximation and the third is the inability to simply develop models to describe non-Newtonian suspending fluid behaviors.

A way to circumvent the use of closure approximation is to directly solve the Fokker-Planck equation in both the spatial and configurational spaces. The implementation of Fokker-Planck equation has already been implemented with different types of numerical tools. Another engineering application, where the PDF is useful, is for fluids in which viscoelasticity is important. Indeed, the PDF can represent the statistics of polymer chain conformations at a given point. For instance, Lozinski and Chauvière [11] investigated the flow of a viscoelastic fluid past a confined cylinder using PDF for the FENE (Finitely Extensible Nonlinear Elastic) model. Moosaie and Manhart [12] proposed a direct simulation to solve the problem of Brownian fiber suspension flows in complex geometries. This procedure yields a direct solution of the Fokker–Planck equation without closure approximation. For homogeneous flows, Férec et al. [13] used a finite volume method to investigate the Folgar–Tucker–Lipscomb model for fiber suspension application. Krochak et

al. [14] and then more recently Johnson et al. [15] developed a numerical simulation of a fiber suspension flow in a convergent geometry in 2D plane using the PDF. Sattari et al. [16] extended the problem in 3D. Mezi et al. [17] have introduced a numerical simulation for 2D planar flows for fiber suspension with a Newtonian and a power-law suspending fluid. They used a finite element method with two 2D meshes. The 2D flow is solved using the first mesh and the second one is the conformational mesh or the orientation mesh which divides the unit circle in 30 parts to represent the number of orientation unknowns. Ammar et al. [18, 19] proposed a new solution technique called PGD (Proper Generalized Decomposition) that allows for the direct solution of the Fokker-Planck equation in conformation spaces of high dimension.

The aim of this paper is to develop a numerical simulation of 2D axisymmetric flows for fiber suspensions using the PDF in 3D. The flow mesh is given by a 2D axisymmetric domain and the conformational mesh is done over the surface of a unit sphere. As the PDF is 3D, the number of unknowns is 900 (i.e., 30×30) for the conformational domain. This paper is organized as follows. The next section is dedicated to the mathematical modeling. Then Section 3 describes the strategy to solve the Fokker-Planck equation on the unit sphere and the fluid mechanics problem on the flow mesh. Finally, before the concluding remarks, three geometries have been investigated: a circular pipe, a center-gated disk and the die swell.

2. Mathematical modeling

The problem is governed by the continuity and Cauchy momentum equations in the limit of creeping flow under the assumptions of an isothermal and incompressible fluid while neglecting body forces

$$\nabla_{\mathbf{x}} \cdot \mathbf{u} = 0, \tag{1a}$$

$$\nabla_{\mathbf{x}} p + \eta_0 \boldsymbol{\Delta}_{\mathbf{x}} \mathbf{u} + \nabla_{\mathbf{x}} \cdot \boldsymbol{\tau} = \mathbf{0}. \tag{1b}$$

In the above equations, p denotes the pressure, η_0 describes the Newtonian viscosity for the suspending fluid, $\mathbf{u}$ is the velocity vector and $\boldsymbol{\tau}$ represents the extra stress tensor arising from the fiber hydrodynamic contribution. The operators $\nabla_{\mathbf{x}}$ and $\boldsymbol{\Delta}_{\mathbf{x}}$ refer to the partial derivative and the Laplacian with respect to the space coordinates $\mathbf{x}$, respectively. In the following, the cylindrical coordinates denoted by r, θ and z are suitable and help to reduce the complexity of the analysis in axisymmetric geometries. Hence, the associated components for the velocity vector are u, v and w.

Several approaches are used for expressing constitutive equations in fiber suspensions [20, 21, 22, 4, 8]. Fibers are generally considered to be slender leading to ignore the particle thickness and are large enough to neglect their Brownian motion. It is also assumed that fibers are represented by rigid cylinders, have a monodisperse distribution in particle length (L) and diameter (D), and exhibit a spatially uniform concentration (i.e., there are no concentration gradients). Therefore, a typical extra stress tensor for fiber suspensions can be expressed as

$$\boldsymbol{\tau} = \eta_0 N_p \dot{\boldsymbol{\gamma}} : \int_{\mathbf{p}} \mathbf{pppp}\ \psi\ d\mathbf{p} = \eta_0 N_p \dot{\boldsymbol{\gamma}} : \langle \mathbf{pppp} \rangle\,, \tag{2}$$

where $\dot{\boldsymbol{\gamma}} = \nabla_{\mathbf{x}}\mathbf{u} + \nabla_{\mathbf{x}}\mathbf{u}^{\dagger}$ is the strain rate tensor ($\dagger$ represents the transpose operator). N_p is a rheological coupling coefficient and various expressions for N_p are available in the literature [23]. N_p generally depends on the particle volume fraction ϕ_f and the fiber aspect ratio $a_r = L/D$. As a first approach and without loss of generality, constant values for N_p are considered in this work.

The orientation of a single fiber is usually given by a unit vector $\mathbf{p}$ aligned along its principal axis (see top-right view object in Fig. 1) and therefore the fourth-order tensor $\langle \mathbf{pppp} \rangle$ describes a fiber orientation statistics in a representative elementary volume [3]. This tensor quantity is connected to the PDF by assuming that all particles in the averaging volume rely upon a population with the same PDF. Hence, for a medium containing a large number of fibers, the time rate of change for the PDF can be written as [17]

$$\dot{\psi} = -\nabla_{\mathbf{x}} \cdot (\dot{\mathbf{r}}_{\mathbf{c}} \psi) - \nabla_{\mathbf{p}} \cdot (\dot{\mathbf{p}} \psi)\,. \tag{3}$$

In the above equation of continuity for ψ, the over-dot symbol refers to the partial time derivative and $\nabla_{\mathbf{p}}$ corresponds to the differential operator on the surface of a unit sphere [24]. The fiber dynamics $\dot{\mathbf{p}}$ is given by the Jeffery equation [1] (in the limit of slender particles) and includes the fiber interactions introduced by Folgar and Tucker [25]. Similar to the Folgar-Tucker idea, the center of the particle $\dot{\mathbf{r}}_{\mathbf{c}}$ is prescribed to translate with the local fluid velocity plus a random perturbation due the particle interactions,$-\mathbf{D}\cdot\nabla_{\mathbf{x}}\log\psi$, where $\mathbf{D}$ is a tensor characterizing diffusion through the perpendicular and parallel directions of the fiber axis. Since a homogenous system is assumed, there are no concentration gradient and therefore $\nabla_{\mathbf{x}}\log\psi=\mathbf{0}$. With these assumptions in mind and including the incompressibility condition, Eq. 3 can be recast as

$$\dot{\psi}+\mathbf{u}\cdot\nabla_{\mathbf{x}}\psi=-\nabla_{\mathbf{p}}\cdot\left[\left(\boldsymbol{\kappa}\cdot\mathbf{p}-\boldsymbol{\kappa}:\mathbf{ppp}\right)\psi\right]+C_I|\dot{\gamma}|\Delta_{\mathbf{p}}\psi, \tag{4}$$

where $\boldsymbol{\kappa}=\boldsymbol{\nabla}_{\mathbf{x}}\mathbf{u}^{\dagger}$ is the transpose of the velocity gradient and the operation analogous to $\Delta_{\mathbf{p}}$ is $\nabla_{\mathbf{p}}\cdot\nabla_{\mathbf{p}}$. C_I represents the interaction coefficient and $|\dot{\gamma}|$ denotes the magnitude of the effective deformation rate (i.e., the second invariant of the strain rate tensor) [25]. Some expressions can be found in the literature [23] and again, without loss of generality, C_I is selected to be a constant in this work.

For homogeneous flows, numerical solutions of Eq. 4, based on the finite volume method discretization, have been checked for stability and convergence over a wide range of values of the interaction coefficient C_I and tested against data available in the literature [13]. This previous work has been extended to solve the full Eq. 4 in 2D planar flows [17], where accuracies in the calculations have been verified. Here, we aim to use the Fokker-Planck, Eq. 5, to predict the flow of fiber suspensions in axisymmetric geometries. The challenge lies in describing the fiber orientation distribution in 3D instead of 2D.

The above governing equations differ from the ones classically used in the literature. Indeed, standard theories for fiber suspensions describe the micro-structure dynamics by a second-order tensor field (instead of using the PDF) such as

$$\dot{\langle\mathbf{pp}\rangle}+\mathbf{u}\cdot\nabla_{\mathbf{x}}\langle\mathbf{pp}\rangle=\boldsymbol{\kappa}\cdot\langle\mathbf{pp}\rangle+\langle\mathbf{pp}\rangle\cdot\boldsymbol{\kappa}^{\dagger}-2\boldsymbol{\kappa}:\langle\mathbf{pppp}\rangle+2C_I|\dot{\gamma}|\left(\boldsymbol{\delta}-3\langle\mathbf{pp}\rangle\right), \tag{5}$$

where $\mathbf{a_2}=\langle\mathbf{pp}\rangle$ and $\mathbf{a_4}=\langle\mathbf{pppp}\rangle$ are in fact the well known orientation tensors [3]. Eq. 5 requires a closure approximation and although various closure approximations have been proposed, their accuracies are difficult to quantify and yield to some questionable results [26, 27, 28].

3. Numerical strategy

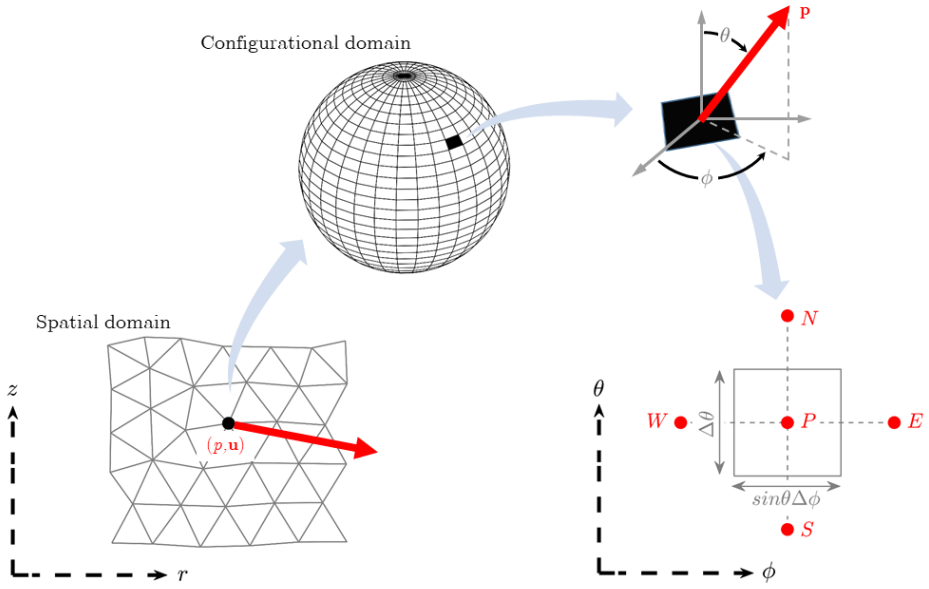

Figure 1: Scheme representing the flow modeling for a fiber suspension using the PDF.

Eq. 4 is a transient convection–diffusion problem with a spatial coordinate dependence (see bottom-left view object in Fig. 1). The solution in the configurational space is performed by using a finite volume method, which has the particularity to use consistent expressions to evaluate convective and diffusive fluxes. The configurational domain is represented on a surface of the unit sphere, which is the field of all possible fiber orientations (see top-left view object in Fig. 1). Hence, this surface is discretized with incremental areas $\Delta A = \sin\theta\ \Delta\theta\ \Delta\phi$, where $\Delta\theta$ and $sin\theta\ \Delta\phi$ are the dimensions of an element on the spherical surface (see bottom-right view object in Fig. 1). At this stage, it is appropriate to establish a system of notation, where P is a general nodal point and its neighbors on the surface of the unit sphere are the west, east, north and south identified by W, E, N and S, respectively. Eq. 4 is then integrated over the control volume to yield to the following discretized equation at its nodal point P

$$\Delta A_P\ \dot{\psi}_P + \Delta A_P\ \mathbf{u}\cdot\nabla_{\mathbf{x}}\psi_P - \Delta A_P\ c_{num}\ \Delta_{\mathbf{x}}\psi_P + a_P\psi_P - a_W\psi_W - a_E\psi_E - a_N\psi_N - a_S\psi_S = 0, \tag{6}$$

where $\Delta A_P = \sin\theta_P\ \Delta\theta\ \Delta\phi$. Férec et al. [13] have provided the expressions for the coefficients a_E, a_W, a_N, a_S and a_P. The third term in Eq. 6 is introduced to stabilize the numerical scheme by adding an artificial isotropic diffusion term proportional to c_{num}. The system of governing equations is solved using the finite element method. Theses equations are implemented in Comsol Multiphysics by taking advantage of the similarity with the coefficient form PDE, presented in the software. Hence, the coefficients in Eq. 6 are identified with the ones for the convection–diffusion problem. Note that the absorption coefficients are introduced with respect to the connectivity table (terms involving the coefficients a_W, a_E, a_N, a_S and a_P) from the mesh in the configurational domain. The weak-form formulation is used to add the fiber stress contribution in the domain and enables to easily couple the velocity and the pressure fields with the fiber stress contribution. The Arbitrary Lagrangian Eulerian (ALE) method is used to perform computations when dealing with a free surface. The spatial discretization of the pressure and velocity fields is done on a P1+P2 element, whereas elements with Lagrangian shape functions of order quadratic are used for ψ.

All the computations were carried out on a workstation Dell PowerEdge R930 with Intel Xeon E7-8860 v4 @ 2.20GHz CPU with 72 threads and 1TB RAM. CPU time depends on the investigated axisymmetric geometries. The circular tube geometry, the flow through the center-gated disk and the die swell problem requires around 9 hours, 1 day and 1 week of computation time, respectively. As much as possible, the mesh is optimized to reduce the number of nodes while preserving the accuracy. For instance, for the pipe problem, the default mesh settings are used (i.e., normal mesh) and boundary layers (thin quadrangles) are generated around no-slip boundaries (see Fig. 2).

For the three flow problems, five types of boundary conditions, denoted by $BC1$ to $BC5$, are prescribed. $BC1$ refers to a inlet velocity profile condition whereas $BC2$ is a outlet condition, where the total normal stress and the shear stress are assumed to vanish. $BC3$ indicates a zero-slip condition and $BC4$ designates a symmetry condition. The $BC5$ boundary condition is only experienced for the die swell problem and signifies the free surface boundary (air-fluid interface), on which the surface tension is neglected. This leads to zero normal and tangential stresses such as $(-p\boldsymbol{\delta} + \eta_0\dot{\boldsymbol{\gamma}} + \boldsymbol{\tau})\cdot\mathbf{n} = \mathbf{0}$, where $\mathbf{n}$ is a outward unit vector normal to the boundary domain. Additionally, a kinematic condition [29] is applied $\frac{\partial h}{\partial t} + w\frac{\partial h}{\partial z} - u = 0$. This last equation is in fact used in order to calculate the unknown position $h(z,t)$ of the free surface. This kinematic condition ensures that the free surface is a streamline, where a particle on the surface has a trajectory that remains on the free surface, $\mathbf{u}\cdot\mathbf{n} = 0$.

This work does not aim to test the effect of the model parameters but to show the possibility of using the 3D probability distribution function in the future to develop more physical modeling, such as particle migration. Hence, parameter values are kept constant over the different simulations such as the suspending fluid viscosity $\eta_0 = 1000\ Pa{\cdot}s$ and the interaction coefficient $C_I = 0.01$. The results presented in this work have been obtained using the artificial numerical diffusion coefficient with $c_{num} = 1\mathrm{E}-10\ m^2/s$, unless otherwise indicated.

4. Flow through a circular pipe

Fiber suspensions flowing in circular tube are encountered in several manufacturing processes and is therefore of interest from a practical viewpoint, but also for validating model implementation. The flow through a pipe is described in Fig. 2, where half of the flow domain is considered, owing to the geometrical symmetry. For this problem, $L = 3R$ is the length of the tube and $R = 1\ m$ is its radius. At the entrance, a laminar inflow ($BC1$) is assumed such as the normal velocity component is given by $w/w_{max} = 1-(r/R)^2$, where the maximum velocity is $w_{max} = 1\ m/s$ and a ($BC2$) boundary condition is applied at the outlet. A zero-slip boundary condition ($BC3$) is applied to the wall and the axisymmetric axis satisfies the symmetry condition ($BC4$). Finally, a completely random distribution of fiber orientation is assumed at the tube entrance and is imposed by a Dirichlet-type boundary condition such as $\psi = 1/(4\pi)$. The domain is discretized using 1495 elements as shown in Fig. 2.

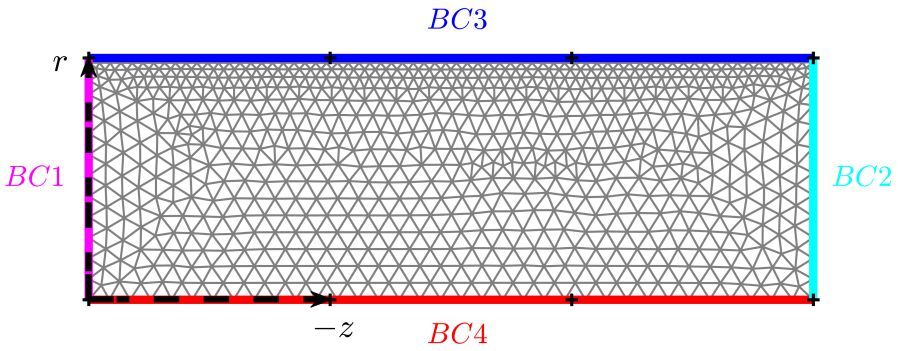

Figure 2: FE mesh for a circular tube: $BC1$ = laminar inflow; $BC2$ = pressure outlet; $BC3$ = zero-slip condition; $BC4$ = symmetry condition.

The fiber orientation prediction is first examined with an uncoupled flow field (i.e., $N_P = 0$), which is assumed to be steady in the entire domain. In this case, all the streamlines are parallel to each other and parallel to the wall, as depicted by the dashed black lines in Fig. 3. Hence, the flow through a pipe is a pure shear flow except on the axisymmetric axis, where the velocity gradient vanishes. The background color in Fig. 3 represents the dimensionless velocity component in the z-direction (i.e., $-w/w_{max}$) in the fluid domain, for which a parabolic distribution is observed. The average fiber orientations are described by ellipses derived from the second-order moments of the PDF. Indeed, the eigenvalues and the eigenvectors of $\mathbf{a_2}$ give the two major axes of the ellipse in the rz-plane and indicate the degree of orientation along these two directions [30]. Furthermore, the filling color for the ellipses (taken from a gray-scale colormap) specifies the magnitude for the eigenvalue in the θ-direction. A white color corresponds to the isotropic value (i.e. 1/3) whereas a black color signifies a value close to 0.17. It can be observed that the fiber orientation is quasi-random close to the symmetrical axis, and the ellipses are flattened and aligned on the other end close to the wall. In this region, a perfect alignment of fibers along the streamlines is not reached since the nonzero value for C_I tends to randomize the orientations, as predicted by the Folgar-Tucker model.

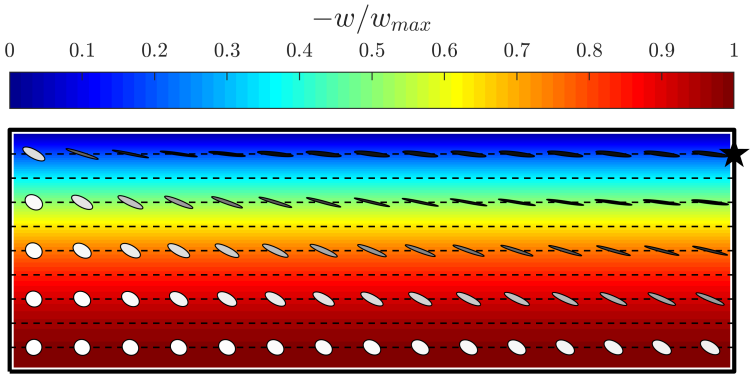

Figure 3: Dimensionless velocity component w in the domain (rz-plane) for a uncoupled solution ($N_p = 0$). Average orientation distributions are represented by ellipses and the black dashed lines are streamlines.

For a fiber suspension flowing through a circular tube, the orientation field can be considered spatially uniform if the coupling effect is ignored (i.e., $N_p = 0$). It means that an observer moving with the fluid allows one to calculate the dynamic orientation history along a streamline, or in other words, the material derivative can be replaced by the total derivative leading to neglect the second term in the right-hand side of Eq. 4. This is known as the single point calculation (SPC) and provides a method for expressing the components of orientation tensors in terms of time (or total deformation, $|\gamma|$) only. Following Férec et al. [8], the a_{rr}, a_{zz} and a_{rz} components are directly computed from the FP equation for 3D orientations with the assumption of a homogeneous shear flow and with prescribing a constant velocity gradient value along a streamline. This calculation is performed by discretizing the half sphere of unit radius into $N = 150 \times 150$ element areas (i.e., ΔA), in contrast to the FE scheme where only $N = 30 \times 30$ element areas are considered. More in detail, $\mathbf{a_2} \approx 2\ \Delta\theta\ \Delta\phi \sum_{i=1}^{N}\ \mathbf{p}_i\mathbf{p}_i\ \sin\theta_i\ \psi_i$, which results from post-treatments. Here, a_{rr} and a_{zz} indicate the fiber orientations in the r- and z-directions, respectively, whereas a_{rz} indicates out-of-plane orientation, from the plane parallel to the r-direction toward the z-direction. Fig. 4 illustrates a comparison between the FE and SPC results for the streamline at $r/R = 0.9$. It can be noticed that the FE results are consistent with the SPC ones in providing the accurate dynamics and the appropriate steady-state conditions. This analysis confirms the well-implementation of the FE code and also the choice for discretizing the configurational domain with 30×30 element areas. An interesting aspect of this test is what would be the fiber orientation distribution if a closure approximation is used. Let consider the invariant based orthotropic fitted closure (IBOF) developed by Chung and Kwon [31], as this closure is generally handled for typical flow fields and is known to be relevant. The IBOF closure is derived from the Caley-Hamilton theorem to yield a general expression of $\mathbf{a_4}$ in terms of $\mathbf{a_2}$ and the identity tensor. The six weighting coefficients depend on the second and third invariant of $\mathbf{a_2}$ since the first invariant is identically equal to 1. It can be shown that there are only three independent coefficients among the six due to simplifications using the normalization and full symmetry conditions. The three remaining coefficients are fit to a fifth-order polynomial combination of the second and third invariants of $\mathbf{a_2}$ and the approximate components of $\mathbf{a_4}$ are compared to the orientation tensors obtained from the PDF. The IBOF procedure is computationally more efficient than that of the orthotropic fitted closure approximations since the costly matrix rotation calculations that are required for the eigenvalue-based closures are avoided by the IBOF closure. Fig. 4 shows again the a_{rr}, a_{zz} and a_{rz} components obtained with the IBOF closure. Although a_{rz} is well predicted, both a_{rr} and a_{zz} exhibit larger overshoots. Furthermore, a_{rr} value is slightly lower while a_{zz} is overestimated as compared with the steady plateau values. Table 1 reports these steady values and gives the absolute relative errors when the SPC results are considered as the reference.

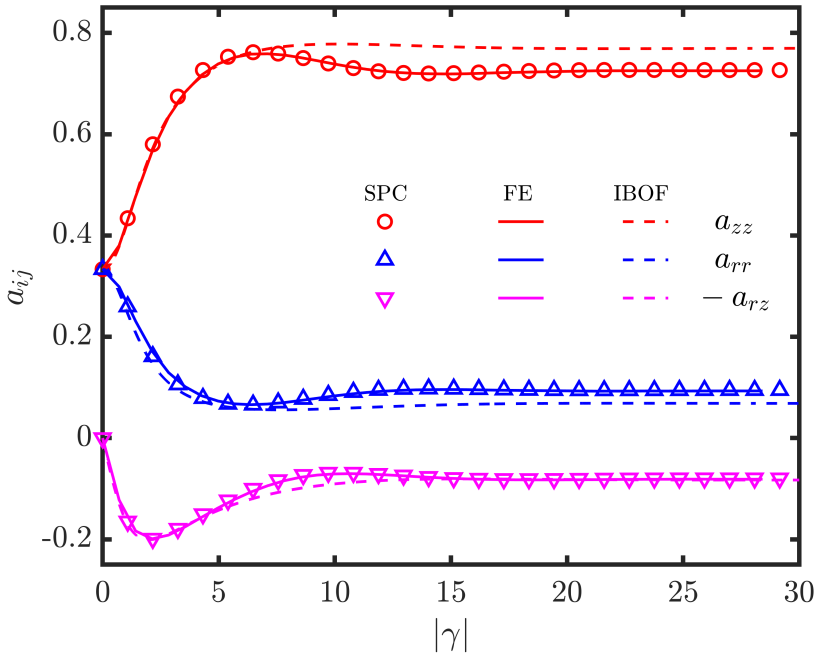

Figure 4: a_{rr}, a_{zz} and a_{rz} versus total strain for the streamline along the line $r = 0.9R$ in a circular tube. FE and SPC designates results from the finite element simulation and from single-point calculations (SPC) (using the FP equation with 150×150 incremental areas), respectively. Predictions obtained with the IBOF closure approximation are also shown. Note that $-a_{rz}$ is plotted instead of a_{rz} for a better clarity.

Table 1: Steady values for a_{rr}, a_{zz} and a_{rz} obtained from SPC, FE and IBOF results and their associated absolute relative errors.

	SPC	FE	ERR_{FE}	IBOF_{in}	$\text{ERR}_{IBOF_{in}}$	IBOF_{out}	$\text{ERR}_{IBOF_{out}}$
a_{rr}	0.0933	0.0931	0.3%	0.0685	26.6%	0.0685	26.6%
a_{zz}	0.7234	0.7253	0.3%	0.7699	6.5%	0.7733	6.9%
a_{rz}	0.0795	0.0812	0.3%	0.0828	4.2%	0.0829	4.3%

Fig. 5a depicts the steady-state fiber orientation distribution obtained from the SPC along the streamline located at $r/R = 0.9$ at the tube exit (represented by a black pentagram in Fig. 3). As the mesh is very fine (i.e., 150×150), this fiber orientation distribution, ψ_{SPC}, is considered to be the reference. In terms of elevation and azimuthal angles, Fig. 5a indicates that most of the fibers are aligned along $\theta \approx \phi \approx 0$ and $\theta \approx \phi \approx \pi$, which correspond to the z-direction. Fig. 5b presents the PDF obtained from the FE simulation at the same location point. As shown in Fig. 6a, the difference between the reference and the FE solutions, $\psi_{SPC} - \psi_{FE}$, is very small (minimum and maximum values of -0.02 and 0.01, respectively).

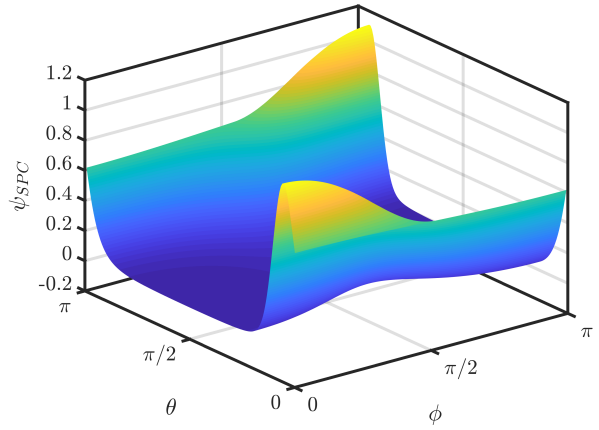

(a) PDF from SPC with a fine mesh of 150×150 element areas.

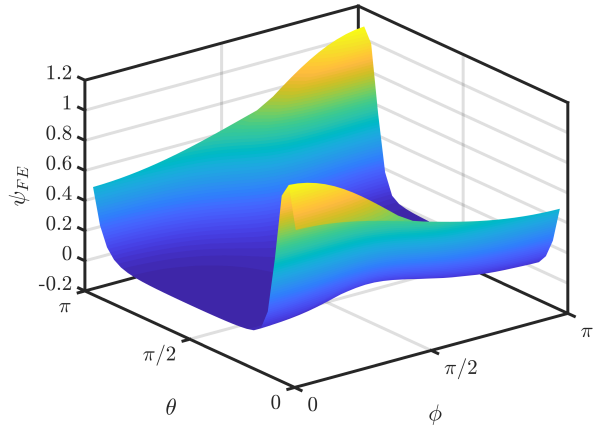

(b) PDF from FE with a mesh of 30×30 element areas.

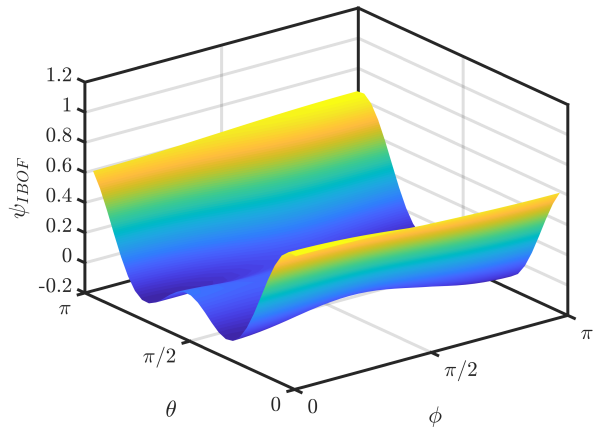

(c) Recovery of the PDF by using the IBOF closure.

Figure 5: PDF located at the tube exit and at $r/R = 0.9$ (represented by a black pentagram in Fig. 3).

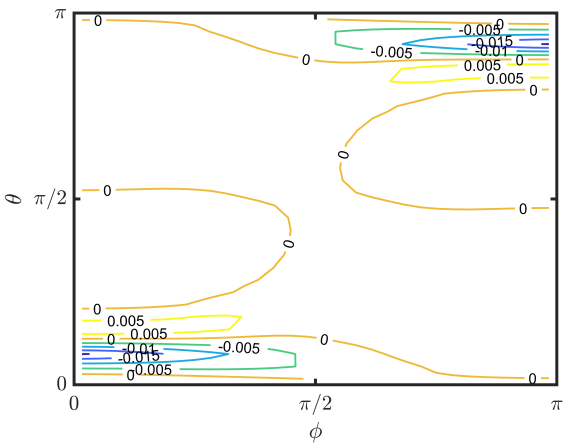

(a) Difference between ψ_{SPC} and ψ_{FE}.

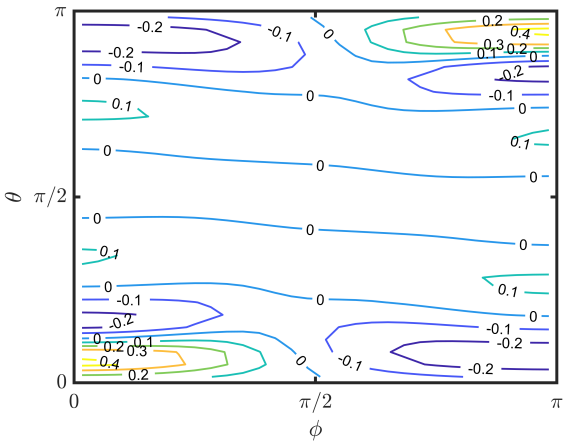

(b) Difference between ψ_{SPC} and ψ_{IBOF}.

Figure 6: PDF difference at the tube exit and at $r/R = 0.9$ (represented by a black pentagram in Fig. 3).

When using the IBOF closure approximation (see Fig. 4), some fiber orientation tensors such as $\mathbf{a_2}$ and $\mathbf{a_4}$ are known (the first one arises from an equation of change, i.e. Eq. 5, and the second one derives from the closure approximation). Therefore, it is possible to recover the PDF based on a Fourier series expansion, where the coefficients transform as tensors under rigid rotations of the material element [32]. By truncate the series beyond the 4th-order terms, it is conceivable to describe the fiber orientation distribution in the following form [3]

$$\psi_{IBOF} \approx \frac{1}{4\pi} + \frac{15}{8\pi}\mathbf{f_2} : \mathbf{b_2} + \frac{315}{32\pi}\mathbf{f_4} :: \mathbf{b_4}, \tag{7}$$

where :: is the scalar product (quadruple contraction) of two fourth-order tensors. Eq. 7 is equivalent to expanding the PDF in orthogonal functions (i.e., spherical harmonics) of the components of $\mathbf{p}$ and therefore $\mathbf{b_2}$ and $\mathbf{b_4}$ represent the deviatoric form of the second- and the fourth-order orientation tensors, respectively.

In terms of index notation, they can be expressed as

$$b_{ij} = \left\langle p_i p_j \right\rangle - \frac{1}{3}\delta_{ij}, \tag{8a}$$

$$b_{ijkl} = \left\langle p_i p_j p_k p_l \right\rangle^{IBOF} - \frac{1}{7}\left(\delta_{ij}\left\langle p_k p_l\right\rangle + \delta_{ik}\left\langle p_j p_l\right\rangle \delta_{il}\left\langle p_j p_k\right\rangle + \delta_{jk}\left\langle p_i p_l\right\rangle + \delta_{jl}\left\langle p_i p_k\right\rangle + \delta_{kl}\left\langle p_i p_j\right\rangle\right) + \frac{1}{35}\left(\delta_{ij}\delta_{kl} + \delta_{ik}\delta_{jl} + \delta_{il}\delta_{jk}\right), \tag{8b}$$

and $\mathbf{f_2}$ and $\mathbf{f_4}$ are their associated tensor basis functions of $\mathbf{p}$ such as

$$f_{ij} = p_i p_j - \frac{1}{3}\delta_{ij}, \tag{9a}$$

$$f_{ijkl} = p_i p_j p_k p_l - \frac{1}{7}\left(\delta_{ij}\left\langle p_k p_l\right\rangle + \delta_{ik}\left\langle p_j p_l\right\rangle \delta_{il}\left\langle p_j p_k\right\rangle + \delta_{jk}\left\langle p_i p_l\right\rangle + \delta_{jl}\left\langle p_i p_k\right\rangle + \delta_{kl}\left\langle p_i p_j\right\rangle\right) + \frac{1}{35}\left(\delta_{ij}\delta_{kl} + \delta_{ik}\delta_{jl} + \delta_{il}\delta_{jk}\right). \tag{9b}$$

To check the accuracy of our calculations, orientation components obtained from Fig. 3 (see Table 1 and column titled IBOF$_{in}$) with the help of the IBOF closure are used as entrance data in the above relationship to reconstruct the fiber orientation distribution, called ψ_{IBOF}. From this PDF, $\mathbf{a_2}$ is recomputed and results are given in Table 1 (column titled IBOF$_{out}$). Both results *in* and *out* are in accordance. Fig. 5c depicts the recovery of the PDF by using the IBOF closure. Negative values are observed, which are unphysical, and in the regions where fibers are closely aligned along the z-direction, the reconstruction of the PDF up to the 4th-order leads to erroneous values, as shown in Fig. 6b (minimum and maximum values of -0.26 and 0.43, respectively). Information given by $\mathbf{a_4}$ is insufficient to represent quasi-aligned distribution, which represents most steady-state solutions for flow-induced orientation. Although all the solutions lead to a close fiber orientation state for $\mathbf{a_2}$, the orientation distribution functions, describing most finely the fiber micro-structure than $\mathbf{a_2}$, may have different shapes.

When the coupling effect is considered (i.e., $N_p \neq 0$ in Eq. 2), the fiber suspension becomes a non-Newtonian fluid since the particle stress contribution appear in the momentum equation (see Eq. 1b). Indeed, anisotropic viscosities are obtained once average fiber orientations leave their 3D random configuration. In Fig.7, a Newtonian profile is observed at the flow inlet imposed by the boundary condition. Since an isotropic orientation is also assumed at $z = 0$, the equivalent viscosity is homogeneous at the tube entrance. Just after the entrance, streamlines are slightly disturbed (leading to extension in the r-direction) and become parallel to each other while approaching the tube exit. Indeed, the velocity profile becomes flatter between the core (along the axisymmetric axis, $-w/w_{max}$ reduces from 1 m/s at the inlet to 0.931 m/s at the outlet), where the orientation is not aligned and the wall where fibers are closely aligned and therefore, the flow manifests a non-Newtonian behavior. In Fig. 7, we recall that the magnitude for the eigenvalue in the θ-direction is related to the filing color for the ellipses. Here, a white color corresponds to 0.35 (i.e., close the isotropic value) whereas a black color indicates a value close to 0.18. In terms of fiber orientation, the coupling between flow and orientation has a negligible effect since a shear flow dominates in this simple geometry. This is not true for the pressure field, which increases when increasing the coupling effect [17].

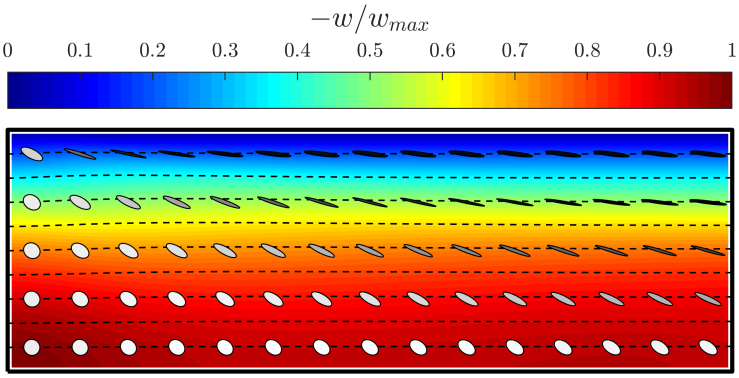

Figure 7: Dimensionless velocity component w in the domain (rz-plane) for a coupled solution ($N_p = 10$). Average orientation distributions are represented by ellipses and the black dashed lines are some streamlines.

5. Center-gated disk flow

This type of flow is frequently encountered in injection molding and therefore is an important test problem for modeling fiber orientation. This radial flow in a disk is a combination of shearing flow in the rz-plane and elongational flow in the $r\theta$-plane. An interesting aspect of this flow geometry is that the region near the boundaries is shear dominant and the region near the mid-plane of the gap is elongation dominant. It results in a transition region in the gap, where shear and elongation are combined. Under this configuration, the flow is 2D but the orientation is 3D.

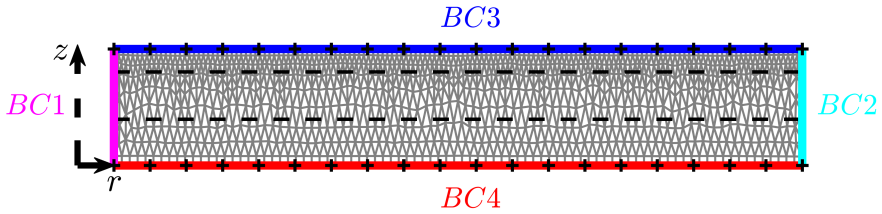

Figure 8: FE mesh for center-gated disk: $BC1$ = laminar inflow; $BC2$ = pressure outlet; $BC3$ = zero-slip condition; $BC4$ = symmetry condition. The black dashed line is parallel to the symmetry centerline at $z/H = 0.4$ and 0.8.

For the problem under consideration, the half-gap-width, H, and the maximum velocity, u_{max}, are used as the length and the velocity scales to nondimensionalize the flow parameters. If a fully developed velocity profile is presumed at the entry of the disk ($BC1$) (see Fig. 8), therefore the dimensionless velocity profile is $u^* = (1 - z^{*2})/r^*$ for an isothermal and Newtonian fluid [33]. This later relationship can be easily integrated to give the position of a material particle as a function of time. If a fluid particle starts at radius $R_i^* = 1$ at time $t^* = 0$ then it stays at a constant height z^* and its radial position is given by

$$r^{*2} = R_i^{*2} + 2t^*(1 - z^{*2}). \tag{10}$$

Then, the velocity gradient tensor can be derived based on the velocity profile and suggests that some of its components are not spatially uniform. It means that each fiber experiences a continuously changing shear and extensional gradient depending on its r and z location. In this work, the orientation structure at large distances from the entry (i.e., $r/H > R_e^* = 20$) is not studied since most transient orientation behaviors are assumed to occur close to the inlet at short radial distances. Since the flow and orientation are symmetric about the mid-plane of the gap ($BC4$), the solution is carried out only in one half of the domain. There is no flow, parallel or perpendicular, at the wall ($BC3$) and at the exit, the boundary condition ($BC2$) is imposed. The geometry of the half disk is discretized into a finite difference grid of triangular and rectangular elements (with a total of 1786 elements), as shown in Fig. 8. The results presented in the following are obtained using an isotropic fiber orientation for the flow entrance and are taken along the radial distance from the inlet gate at three different locations through the thickness, $z^* = z/H = 0$, 0.4 and 0.8 (see the black dashed lines parallel to the wall in Fig. 8). In this case, the artificial numerical diffusion coefficient, c_{num}, is set to $1E-7\ m^2/s$ for the spatial diffusion in the FP equation (see Eq. 6).

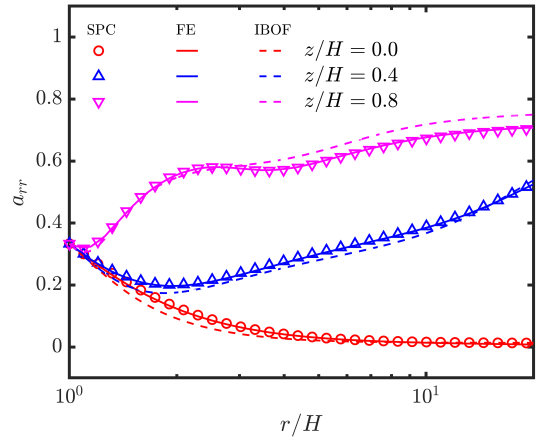

(a) a_{rr} versus r/H

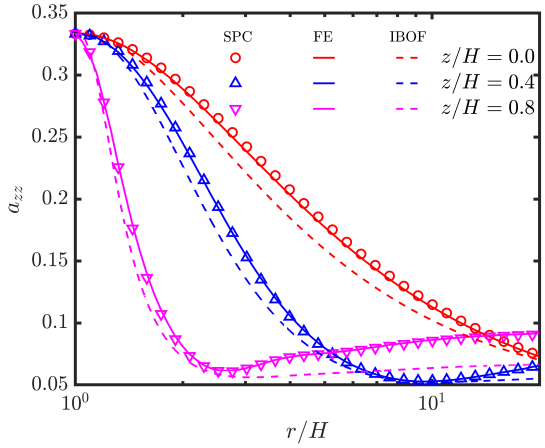

(b) a_{zz} versus r/H

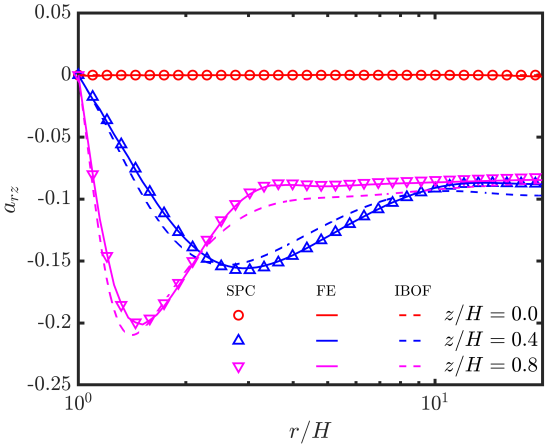

(c) a_{rz} versus r/H

Figure 9: Variation of orientation tensor components with respect to the radial distance r/H at three different z/H locations through the gap width.

Figs. 9a and 9b depict the tensor components for a_{rr} and a_{zz} at three different z/H locations through the gap width in a center-gated disk. For $z/H = 0$ and 0.4, the stretching flow dominates at small radii and therefore a_{rr} and a_{zz} decrease as fibers rotate transverse to the flow. After a certain radial location, the flow at $z/H = 0.4$ becomes shear dominant and a_{zz} increases monotonically. Indeed, at larger radii the ratio of shear rate to stretch rate increases, and the dominant orientation shifts towards the flow direction. At the height of $z/H = 0.8$, a_{rr} increases due to the shear in the rz-plane and is still increasing at R_e^*. The non-zero value for the fiber interaction coefficient maintains a small amount of out-of-plane orientation, as graphed in Fig. 9c, even for very large strains. This keeps the fibers susceptible to the shearing flow, which tends to rotate the fibers towards the radial direction. If fiber-fiber interactions are negligible (i.e., $C_I = 0$), the shearing flow will cause fibers to lie almost flat in the rz-plane with a_{rz} tending to zero.

As done in the previous flow simulations, numerical solutions for the PDF are obtained by integrating the Fokker-Planck equation following a material point [13]. At each time, Eq. 10 gives the radial position of the material point from which the local velocity gradients are deduced. All calculations are performed by using 150×150 element areas and run from $R_i^* = 1$ to $R_e^* = 20$. It is seen that the difference in the predictions between FE and SPC results through the thickness is very small, leading again to validate the numerical implementation. As illustrated in Fig. 9, it is worth mentioning that the IBOF closure approximation does a good job of matching the exact results. It should be noted that both orientation components a_{rr} and a_{zz} would reach a steady-state value at a larger radial distance than depicted in Fig. 9 and Fig. 10.

Fig. 10 shows the predicted orientation results using the uncoupled ($N_p = 0$) and the coupled ($N_p = 10$) solutions at three distinct locations through the thickness (i.e., $z^* = z/H = 0$, 0.4 and 0.8). Although the developing flow field is quantitatively different for both cases, the orientation states are qualitatively similar because the flow field is still elongation dominant near the centerline and shear dominant near the wall. Similar behaviors have been observed by Ranganathan and Advani [34], who showed in addition that a uniform velocity profile at the flow inlet exhibits a more pronounced difference between the coupled and uncoupled approaches. Lastly, we would like to point out that Altan and Rao [33] provided an analytical solution for the 3D orientation distribution function in a center-gated disk for slender fibers in which they neglected particle interactions (i.e., $C_I = 0$).

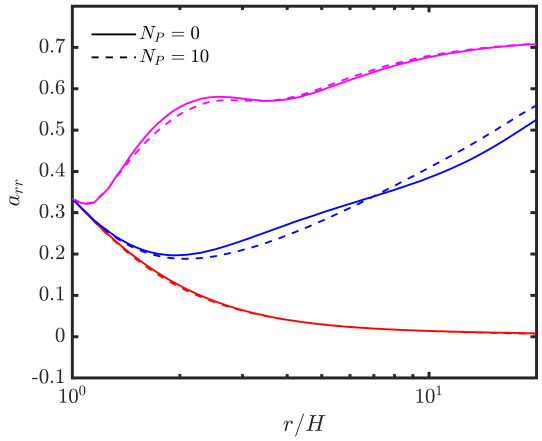

(a) a_{rr} versus r/H

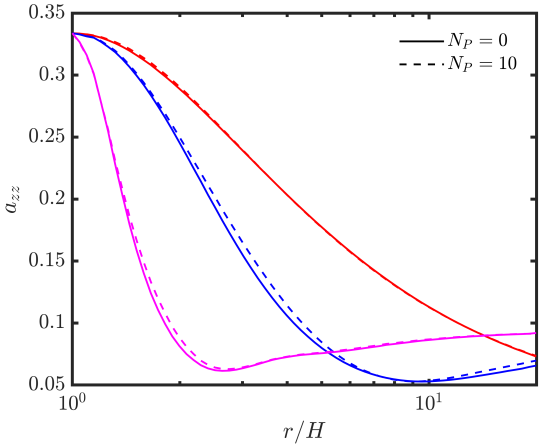

(b) a_{zz} versus r/H

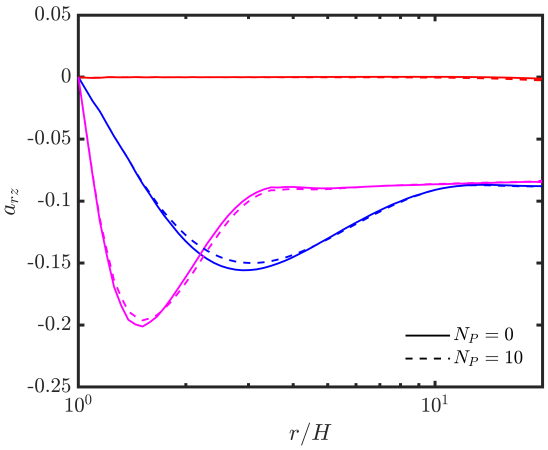

(c) a_{rz} versus r/H

Figure 10: Comparison between uncoupled (N_p = 0) and coupled (N_p = 10) solutions for the orientation components at three different z/H locations through the gap width.

6. Die swelling flow

The die swell phenomenon occurs when a polymer liquid, discharged from channel, experiences free surface flow. The axisymmetric extrudate swell flow of a fiber suspension plays an important role in the industrial application (i.e., capillary/slit type process or extrusion) and is therefore investigated numerically using the 3D PDF.

Fig. 11 illustrates the geometry of the axisymmetric die swell along with the boundary conditions. Note that a fully developed parabolic profile (i.e., $w = w_{max}\left[1-(r/r_0)^2\right]$, where $w_{max} = 10^{-4}\ m/s$) and a random fiber orientation are imposed at the die inlet ($BC1$). The die radius is $r_0 = 0.25\ mm$ and the die length and the extrudate swell is taken to be $3.6r_0$ and $5r_0$, respectively. This domain dimension is based on the geometry of the 3D printer nozzle from E3D [35] and is discretized using 839 elements. It is worth mentioning that since the flow domain evolves with time, Eq. 4 solves a 5D problem, two spatial coordinates r and z, two configurational coordinates θ and ϕ, and time t (a time step (of unit time) which is chosen). Fig. 11 (on the left) presents the final mesh once the evolution of the flow domain determined by the kinematic equation has converged.

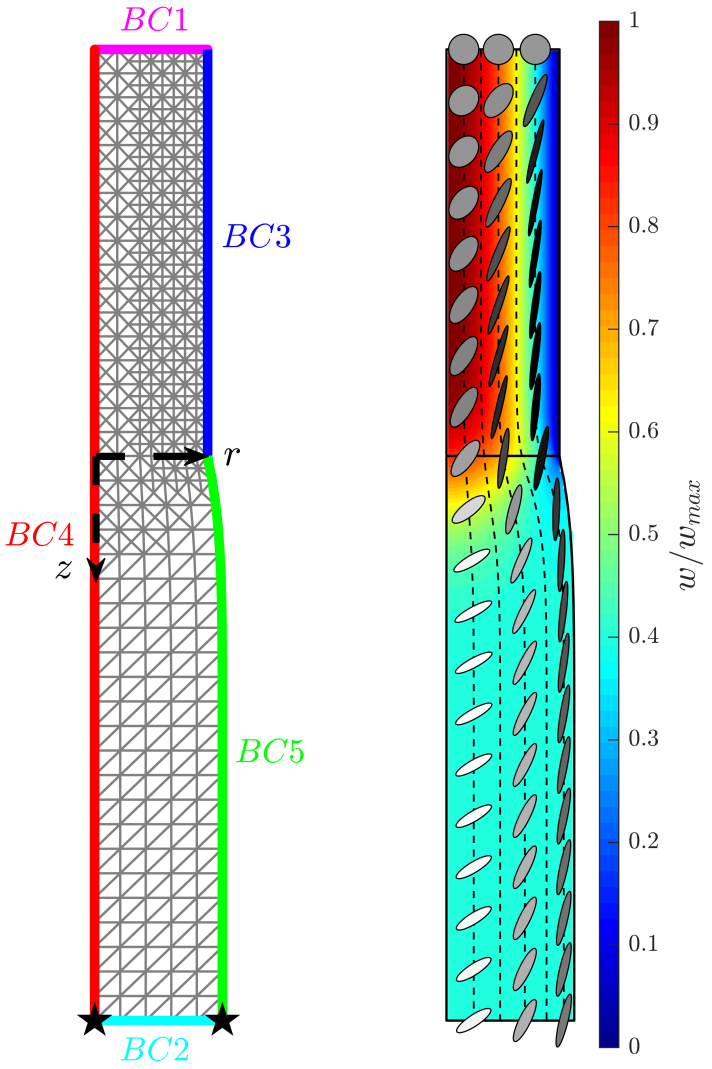

Figure 11: On the left) FE mesh for a die swell problem: $BC1$ = laminar inflow; $BC2$ = pressure outlet; $BC3$ = zero-slip condition; $BC4$ = symmetry condition; $BC5$ = free surface. On the right) Dimensionless velocity component w in the domain (rz-plane) for a uncoupled solution ($N_p = 0$). Average orientation distributions are represented by ellipses and the black dashed lines are some streamlines.

The background color, shown in Fig. 11 (on the right), represents the dimensionless components w of the velocity field for the axisymmetric creeping die swell flow for a fiber suspension without coupling (i.e., $N_p = 0$). Some streamlines are also depicted in this figure as well as the fiber orientation distribution (described by ellipses), which indicates the degree of orientation along every direction. Note that the filling color for the ellipses (taken from a gray-scale colormap) specifies the magnitude for the eigenvalue in the θ-direction. A white color corresponds to the value of 0.438 whereas a black color signifies a value close to

0.181. It can be noted that the fiber orientation distribution inside the die is similar to what is observed within the tube geometry. Immediately after the die exit and close to the centerline, a_{zz} component of the fiber orientation tensor decreases, which is explained by the negative elongation in the z-direction and an expansion in the r-direction, both of which decrease the fiber alignment in the z-direction. On the opposite side close to the free surface, fibers along streamlines exhibit a slight misalignment over a short distance (in the region where $z \approx 0$) as the magnitude of the elongation velocity gradient rapidly exceeds that for radial expansion and therefore a_{zz} increases similar to streamlines close to the centerline. Since the magnitude of the fluid velocity is greater at the center of the die, the elongation flow causes fibers close to the centerline to align faster in the r-direction than fibers close to the free surface. This effect causes decrease of fiber alignment along the flow direction at the die exit to be greater than other streamlines further from the centerline of the die.

Usually the swell is characterized by a measurable parameter $\chi = r/r_0$ presented as the ratio of cross sectional areas of extrudate to the die. Fig. 12 depicts χ with respect to the dimensionless z variable when using the coupled and decoupled approaches. For the case where $N_p = 0$, a final extrudate swell of $\chi = 1.13$ agrees well with the results obtained by Mezi et al. [35] (denoted by Ref. in Fig. 12). The same observation can be made for the coupled model, which has a higher value for χ. Based on the same mesh grid, the same calculations are performed by using the IBOF closure approximation and the tensor representation. It is found that FE and IBOF solutions have the same tendencies. The discrepancies observed with the reference solutions are explained by a finer mesh grid close to the die exit.

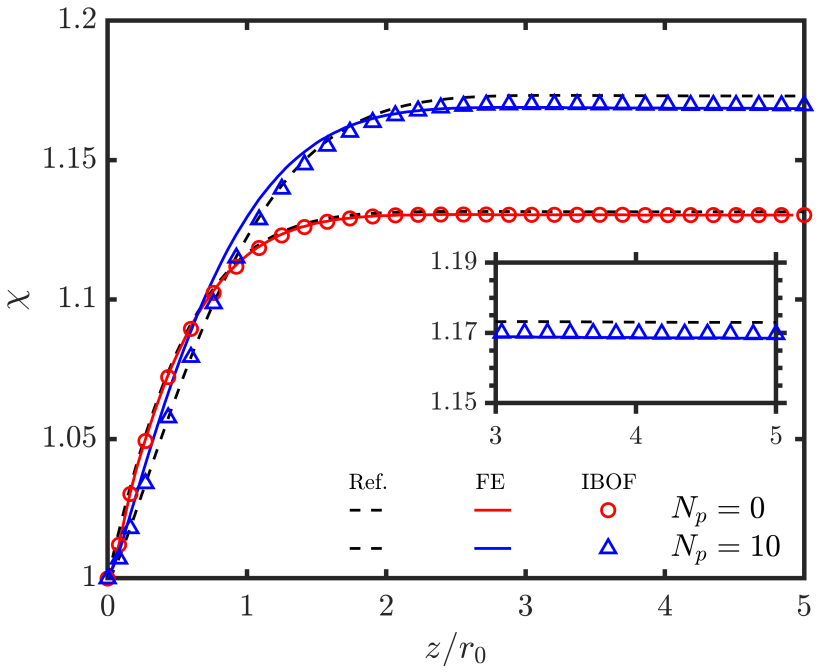

Figure 12: Die swell ratio versus relative abscissa for uncoupled and coupled solutions obtained from FE and IBOF analyses. The insert is a zoom of the steady values for the coupled solutions.

Lastly, Fig. 13 depicts two steady-state fiber orientation distributions obtained from the FE calculation. At $z/r_0 = 5$, two different locations are selected along the free surface and the centerline, respectively. Both locations are represented by a black pentagram on the right in Fig. 11. For the location point on the free surface, Fig. 13a is found to be similar to Fig. 5b, giving the fiber orientation distribution close to the

tube wall at the exit. On the contrary and as discussed before, the PDF located point on the centerline (see Fig. 13b) clearly differs from the previous one and shows that most fibers are aligned along the radial direction.

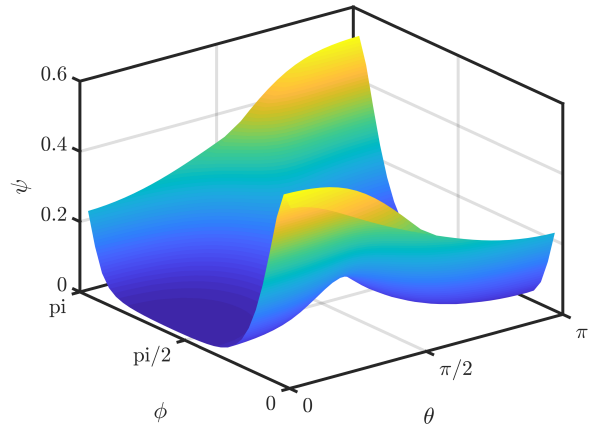

(a) PDF along the free surface at $z/r_0 = 5$.

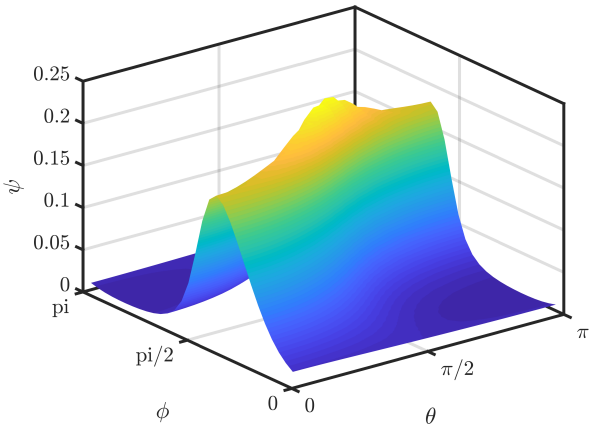

(b) PDF along the centerline at $z/r_0 = 5$.

Figure 13: PDF from FE with a mesh of 30×30 element areas for $N_p = 0$.

7. Concluding remarks

The flow and orientation of a fiber suspension are studied in three axisymmetric flow geometries. The momentum equations and the evolution equation for the 3D probability distribution orientation are coupled with flow using a rheological constitutive equation and solved using a finite element method. The IBOF closure approximation is found to match relatively well the fiber orientation results when compared with the probability distribution function. Differences between the orientation distributions using the coupled and decoupled approaches are not significant except for the velocity field solutions. In particular, the die swell ratio increases with increasing the coupling coefficient when fibers are randomly distributed at the flow inlet.

This numerical approach can be useful to test the accuracies of recent or forthcoming closure approximations. It will be also possible to explore the flow predictions for viscoelastic fluids, for fibers suspended in generalized Newtonian fluids [8, 36] and viscoelastic fluids [10], for interacting fibers [23, 37], for problems involving long and semi-flexible fibers [38, 39] or nanotubes [40], without being hampered by errors arising due to the use of closure approximations. More generally, it will be very helpful for developing new constitutive models involving probability distribution function.

8. Acknowledgments

DM particularly wishes to acknowledge the Brittany Region and the Morbihan subdivision for their financial support.

References

References

[1] G. B. Jeffery, The motion of ellipsoidal particles immersed in a viscous fluid, Proceedings of the Royal Society of London 102 (1922) 161–179. doi:10.1098/rspa.1922.0078.

[2] S. M. Dinh, R. C. Armstrong, A rheological equation of state for semiconcentrated fiber suspensions, Journal of Rheology 28 (3) (1984) 207–227. doi:10.1122/1.549748.

[3] S. G. Advani, C. L. Tucker, The use of tensors to describe and predict fiber orientation in short fiber composites, Journaml of Rheology 31 (8) (1987) 751–784. doi:10.1122/1.549945.

[4] G. G. Lipscomb, M. M. Denn, D. U. Hur, D. V. Boger, The flow of fiber suspensions in complex geometries, Journal of Non-Newtonian Fluid Mechanics 26 (3) (1988) 297–325. doi:10.1016/0377-0257(88)80023-5.

[5] J. Férec, G. , M.-C. Heuzey, P. J. Carreau, Modeling fiber interactions in semiconcentrated fiber suspensions, Journal of Rheology 53 (1) (2009) 49–72. doi:10.1122/1.3000732.

[6] M. Djalili-Moghaddam, S. Toll, A model for short-range interactions in fibre suspensions, Journal of Non-Newtonian Fluid Mechanics 132 (1) (2005) 73 – 83. doi:10.1016/j.jnnfm.2005.08.014.

[7] J. Férec, E. Abisset-Chavanne, G. Ausias, F. Chinesta, On the use of interaction tensors to describe and predict rod interactions in rod suspensions, Rheologica Acta 53 (5-6) (2014) 445–456. doi:10.1007/s00397-014-0767-1.

[8] J. Férec, E. Bertevas, B.-C. Khoo, G. Ausias, N. Phan-Thien, The effect of shear-thinning behaviour on rod orientation in filled fluids, Journal of Fluid Mechanics 798 (1) (2016) 350–370. doi:10.1017/jfm.2016.323.

[9] D. Borzacchiello, E. Abisset-Chavanne, F. Chinesta, R. Keunings, Orientation kinematics of short fibres in a second-order viscoelastic fluid, Rheologica Acta 55 (5) (2016) 397–409. doi:10.1007/s00397-016-0929-4.

[10] J. Férec, E. Bertevas, B.-C. Khoo, G. Ausias, N. Phan-Thien, Steady-shear rheological properties for suspensions of axisymmetric particles in second-order fluids, Journal of Non-Newtonian Fluid Mechanics 239 (2017) 62–72. doi:10.1016/j.jnnfm.2016.12.006.

[11] A. Lozinski, C. Chauvière, A fast solver for fokker–planck equation applied to viscoelastic flows calculations: 2d fene model, Journal of Computational Physics 189 (2) (2003) 607 – 625. doi:10.1016/S0021-9991(03)00248-1.

[12] A. Moosaie, M. Manhart, A direct numerical simulation method for flow of brownian fiber suspensions in complex geometries, Journal of Dispersion Science and Technology 34 (3) (2013) 427–440. doi:10.1080/01932691.2011.634750.

[13] J. Férec, M. Heniche, M.-C. Heuzey, G. Ausias, P. J. Carreau, Numerical solution of the Fokker-Planck equation for fiber suspensions: Application to the Folgar-Tucker-Lipscomb model, Journal of Non-Newtonian Fluid Mechanics 155 (1-2) (2008) 20–29. doi:10.1016/j.jnnfm.2008.04.004.

[14] P. J. Krochak, J. A. Olson, D. M. Martinez, Fiber suspension flow in a tapered channel: The effect of flow/fiber coupling, International Journal of Multiphase Flow 35 (7) (2009) 676–688. doi:10.1016/j.ijmultiphaseflow.2009.03.005.

[15] T. Johnson, P. Roytta, A. Mark, F. Edelvik, Simulation of the spherical orientation probability distribution of paper fibers in an entire suspension using immersed boundary methods, Journal of non-Newtonian Fluid Mechanics 229 (2016) 1–7. doi:10.1016/j.jnnfm.2016.01.001.

[16] M. Sattari, J. Tuomela, H. Niskanen, J. Hamalainen, Coupled simulation of the spherical angles of rigid fibres by using a fibre orientation probability distribution model, International Journal of Multiphase Flow 65 (2014) 61–67. doi:10.1016/j.ijmultiphaseflow.2014.06.002.

[17] D. Mezi, G. Ausias, S. G. Advani, J. Férec, Fiber suspension in 2D nonhomogeneous flow: The effects of flow/fiber coupling for newtonian and power-law suspending fluids, Journal of Rheology 63 (3) (2019) 405–418. doi:10.1122/1.5081016.

[18] A. Ammar, B. Mokdad, F. Chinesta, R. Keunings, A new family of solvers for some classes of multidimensional partial differential equations encountered in kinetic theory modeling of complex fluids, Journal of Non-Newtonian Fluid Mechanics 139 (3) (2006) 153–176. doi:10.1016/j.jnnfm.2006.07.007.

[19] A. Ammar, B. Mokdad, F. Chinesta, R. Keunings, A new family of solvers for some classes of multidimensional partial differential equations encountered in kinetic theory modelling of complex fluids: Part II: Transient simulation using space-time separated representations, Journal of Non-Newtonian Fluid Mechanics 144 (2) (2007) 98–121. doi:10.1016/j.jnnfm.2007.03.009.

[20] G. K. Batchelor, The stress system in a suspension of force-free particles, Journal of Fluid Mechanics 41 (3) (1970) 545–570. doi:10.1017/S0022112070000745.

[21] G. K. Batchelor, The stress generated in a non-dilute suspension of elongated particles by pure straining motion, Journal of Fluid Mechanics 46 (4) (1971) 813–829. doi:10.1017/S0022112071000879.

[22] E. J. Hinch, L. G. Leal, Constitutive equations in suspension mechanics. Part 2. Approximate forms for a suspension of rigid particles affected by brownian rotations, Journal of Fluid Mechanics 76 (1) (1976) 187–208. doi:10.1017/S0022112076003200.

[23] J. Férec, G. Ausias, Rheological modeling of non-dilute rod suspensions, in: F. Chinesta, G. Ausias (Eds.), Rheology of Non-Spherical Particle Suspensions, Elsevier, 2015, pp. 77–117. doi:10.1016/B978-1-78548-036-2.50004-6.

[24] R. B. Bird, C. F. Curtiss, R. C. Armstrong, O. Hassager, Dynamics of polymeric liquids. Volume 2, Kinetic theory, 2nd Edition, Wiley, New York, 1987.

[25] F. Folgar, C. L. Tucker, Orientation behavior of fibers in concentrated suspensions, Journal of Reinforced Plastics and Composites 3 (2) (1984) 98–119. doi:10.1177/073168448400300201.

[26] J. S. Cintra, C. L. Tucker, Orthotropic closure approximations for flow-induced fiber orientation, Journal of Rheology 39 (6) (1995) 1095–1122. doi:10.1122/1.550630.

[27] F. Dupret, V. Verleye, Modeling the flow of fiber suspensions in narrow gaps, in: D. A. Siginer, D. De Kee, R. P. Chhabra (Eds.), Advances in the Flow and Rheology of Non-Newtonian Fluids, rheology ser 8 Edition, Vol. 2, Elsevier, Armsterdam, 1999, pp. 19–29.

[28] D. H. Chung, T. H. Kwon, Improved model of orthotropic closure approximation for flow induced fiber orientation, Polymer Composites 22 (5) (2001) 636–649. doi:10.1002/pc.10566.

[29] R. Keunings, An algorithm for the simulation of transient flows with free surfaces, Journal of Computational Physics 62 (1986) 199–220. doi:10.1016/0021-9991(86)90107-5.

[30] M. C. Altan, S. Subbiah, S. I. Güçeri, R. B. Pipes, Numerical prediction of three-dimensional fiber orientation in Hele-Shaw flows, Polymer Engineering & Science 30 (14) (1990) 848–859. doi:10.1002/pen.760301408.

[31] D. H. Chung, T. H. Kwon, Invariant-based optimal fitting closure approximation for the numerical prediction of flow-induced fiber orientation, Journal of Rheology 46 (1) (2002) 169–194. doi:10.1122/1.1423312.

[32] E. T. Onat, F. A. Leckie, Representation of mechanical behavior in the presence of changing internal structure, Journal of Applied Mechanics 55 (1) (1988) 1–10. doi:10.1115/1.3173630.

[33] M. C. Altan, B. N. Rao, Closed-form solution for the orientation field in a center-gated disk, Journal of Rheology 39 (3) (1995) 581–599. doi:10.1122/1.550714.

[34] S. Ranganathan, S. G. Advani, A simultaneous solution for flow and fiber orientation in axisymmetric diverging radial flow, Journal of Non-Newtonian Fluid Mechanics 47 (1993) 107–136. doi:10.1016/0377-0257(93)80047-F.

[35] D. Mezi, G. Ausias, Y. Grohens, J. Férec, Numerical simulation and modeling of the die swell for fiber suspension flows, Journal of Non-Newtonian Fluid Mechanics 274 (2019) 104205. doi:10.1016/j.jnnfm.2019.104205.

[36] J. Férec, E. Bertevas, B. C. Khoo, G. Ausias, N. Phan-Thien, A rheological constitutive model for semiconcentrated rod suspensions in Bingham fluids, Physics of Fluids 29 (7) (2017) 073103. doi:10.1063/1.4995436.

[37] S. Bounoua, E. Lemaire, J. Férec, G. Ausias, P. Kuzhir, Shear-thinning in concentrated rigid fiber suspensions: Aggregation induced by adhesive interactions, Journal of Rheology 60 (6) (2016) 1279–1300. doi:10.1122/1.4965431.

[38] U. Strautins, A. Latz, Flow-driven orientation dynamics of semiflexible fiber systems, Rheologica Acta 46 (8) (2007) 1057–1064. doi:10.1007/s00397-007-0194-7.

[39] G. M. Lambert, D. G. Baird, Evaluating Rigid and Semiflexible Fiber Orientation Evolution Models in Simple Flows, Journal of Manufacturing Science and Engineering 139 (3), 031012 (10 2016). doi:10.1115/1.4034664.

[40] G. Natale, N. K. Reddy, G. Ausias, J. Férec, M. C. Heuzey, P. J. Carreau, Rheo-optical response of carbon nanotube suspensions, Journal of Rheology 59 (2) (2015) 499–524. doi:10.1122/1.4907743.